


LETTER

Open Access



Dual-band polarized upconversion photoluminescence enhanced by resonant dielectric metasurfaces

Ziwei Feng^{1,2†}, Tan Shi^{1†}, Guangzhou Geng^{3†}, Junjie Li^{3*}, Zi-Lan Deng^{1*}, Yuri Kivshar^{4,5*} and Xiangping Li^{1*} 

Abstract

Lanthanide-doped upconversion nanoparticles emerged recently as an attractive material platform underpinning a broad range of innovative applications such as optical cryptography, luminescent probes, and lasing. However, the intricate 4f-associated electronic transition in upconversion nanoparticles leads only to a weak photoluminescence intensity and unpolarized emission, hindering many applications that demand ultrabright and polarized light sources. Here, we present an effective strategy for achieving ultrabright and dual-band polarized upconversion photoluminescence. We employ resonant dielectric metasurfaces supporting high-quality resonant modes at dual upconversion bands enabling two-order-of-magnitude amplification of upconversion emissions. We demonstrate that dual-band resonances can be selectively switched on polarization, endowing cross-polarization controlled upconversion luminescence with ultra-high degrees of polarization, reaching approximately 0.86 and 0.91 at dual emission wavelengths of 540 and 660 nm, respectively. Our strategy offers an effective approach for enhancing photon upconversion processes paving the way towards efficient low-threshold polarization upconversion lasers.

[†]Ziwei Feng, Tan Shi and Guangzhou Geng are contributed equally to this work.

*Correspondence:

Junjie Li

jjli@phy.ac.cn

Zi-Lan Deng

zilandeng@jnu.edu.cn

Yuri Kivshar

yuri.kivshar@anu.edu.au

Xiangping Li

xiangpingli@jnu.edu.cn

¹ Guangdong Provincial Key Laboratory of Optical Fiber Sensing and Communications, Institute of Photonics Technology, Jinan University, Guangzhou 511443, China

² Wuhan National Laboratory for Optoelectronics, Huazhong University of Science and Technology, Wuhan 430074, China

³ Beijing National Laboratory for Condensed Matter Physics, Institute of Physics, Chinese Academy of Sciences, Beijing 100190, China

⁴ Nonlinear Physics Centre, Research School of Physics, Australian National University, Canberra, ACT 2601, Australia

⁵ Qingdao Innovation and Development Center of Harbin Engineering University, Qingdao 266000, China

1 Introduction

Lanthanide-doped upconversion nanoparticles (UCNPs) demonstrate many superior properties of broadly-tunable multicolor emission and long emission lifetimes making them well-suited for many applications including super-resolution imaging [1–5], optical multiplexing [6, 7], three-dimensional displays [8], and low-threshold lasing [9, 10]. Despite many advantages, the further progress and practical applications of UCNPs face significant challenges due to low upconversion efficiencies. Polarization, being another important characteristic of fluorescence, provides orientation and structural information in an additional dimension, and it has been extensively employed in the fluorescence polarization imaging technique [11, 12]. Unfortunately, the inherent upconversion emission processes associated with the 4f electronic transition in UCNPs are typically weak, and they do not exhibit polarization characteristics [13].

A majority of the previous studies focused primarily on enhancing the upconversion luminescence by coupling

UCNPs with plasmonic nanostructures [14–22]. The concentrated electromagnetic field in the vicinity of these nanostructures can significantly boost both the absorption cross-sections and the upconversion radiation rates. Metallic structures supporting surface plasmons are effective in localizing light and creating strong electric fields, which can enhance upconversion fluorescence. However, metallic nanostructures generally have low values of the quality factor (Q factor) due to the intrinsic loss and may cause quenching effect due to the direct contact to the emission materials. The Q value is a crucial parameter for resonant excitation. The typical range of Q factor for plasmonic resonances is up to a few tens [23]. Although some special designs like metal-insulator-metal (MIM) structure can obtain the high Q factor, the emitters are close to the metallic surface, the quenching effect makes the quantum efficiency drop rapidly. In the meantime, there are also a few works reporting the controllability of luminescence's polarization state with plasmonic structures [24], but the fluorescence enhancement is very weak due to their low Q factor. In addition, these studies have concentrated on the polarization properties of the overall luminescence, which cannot achieve selective modulation of polarization characteristics for multi-color upconversion bands.

In comparison to plasmonic nanostructures, all-dielectric resonant metasurfaces composed of high-index dielectric nanostructures with low losses at visible frequencies support much richer multipolar Mie-resonances [25–30], which provide an excellent alternative to fluorescence enhancement. Furthermore, collective high-Q resonances such as lattice resonances and bound states in the continuum (BICs) emerge due to a coupling of these Mie multipoles in periodic arrays [31–34]. Among them, BICs, which are completely decoupled from radiative modes, have recently attracted considerable attention due to their infinitely-high Q factors [33, 35]. Breaking symmetry of meta-atoms can transform a BIC into a quasi-BIC with finite but extraordinarily high Q factors [36–39]. These emerging concepts have recently been well-exploited and demonstrated for fluorescence enhancement and low-threshold lasing applications [40–42].

Here, we utilize the emerging concept of high-Q collective modes of resonant metasurfaces for polarization-controlled dual-band upconversion burst as illustrated in Fig. 1. We design and fabricate high-Q resonant metasurfaces composed of Titanium dioxide (TiO₂) diatomic nanobricks (Fig. 1a, b), which support a quasi-BIC mode (with $Q \sim 1031$) at the wavelength of 660 nm for the y -polarized incidence, and another high-Q Mie resonance mode (with $Q \sim 1044$) at the wavelength of 540 nm for the x -polarized incidence, respectively. Consequently,

NaYF₄:Yb/Er UCNPs deposited on the metasurface exhibit ultrabright upconversion luminescence at dual bands of 540 and 660 nm, with enhancement factors up to approximately 51-fold and 43-fold. By controlling the rotation of the polarization analyzer, we demonstrate linearly- and cross-polarized emission at dual bands with ultra-high degrees of polarization (DoPs). Our demonstration paves the way for efficient enhancements and polarization control of the UCNP emission with potential applications in low-threshold polarization upconversion lasers and hyperspectral imaging/sensing.

2 Results and discussion

The unit-cell of the proposed dielectric resonant metasurface is shown in Fig. 1b. It is constructed by a pair of TiO₂ (refractive indexes refer to Additional file 1: Fig. S1) nanobricks placed on a SiO₂ substrate. The nanobricks are of height (h) 450 nm, length (w_y) 240 nm and width (w_x) 100 nm. The periods along the x - and y -directions are $p_x = 430$ nm, and $p_y = 345$ nm, respectively. A BIC can be formed in such metasurface without any radiation due to symmetry protection or destructive interference between different radiation channels. In our design, the introduction of the asymmetric parameter δ (the orientation angle δ of the nanobrick with respect to the y axis) breaks the rotational symmetry protection of BICs, transferring them into high Q-factor quasi-BICs that are accessible with free-space excitations at normal incidence. By varying the orientation angle between the two nanobricks and the background refractive index, we can adjust the resonant wavelength to match the emission wavelength of the UCNPs. As depicted in Fig. 1c–e, NaYF₄:Yb/Er (20/2 mol %) nanoparticles with size of around 15 nm (Additional file 1: Fig. S2) were selected to be spin-coated onto the metasurface to adjust the background refractive index. The designed metasurface exhibits a quasi-BIC mode at $\lambda \approx 660$ nm for y -polarization, and another Mie resonance mode at $\lambda \approx 540$ nm for x -polarized light. Those two high-Q resonance modes overlap with the emission band of the Er³⁺ upconversion transition (⁴H_{11/2} to ⁴I_{15/2} and ⁴F_{9/2} to ⁴I_{15/2}).

To further get insights into the resonance behavior, we calculate the reflectance spectra of the metasurface with respect to asymmetry parameter δ under x - and y - polarized normal incidence (Fig. 2a–b). Under y -polarized normal incidence, the metasurface supports a symmetry-protected BIC at $\delta = 0^\circ$, which has an infinite Q-factor indicated by the red circle. A slight symmetry breaking ($\delta \neq 0^\circ$) can transfer the symmetry-protected BIC into a quasi-BIC. Additional file 1: Fig. S3 shows the Q-factor and the resonance wavelength of the quasi-BIC mode on different asymmetry parameter δ . As the δ increases, the Q factor remains high and the resonance wavelength

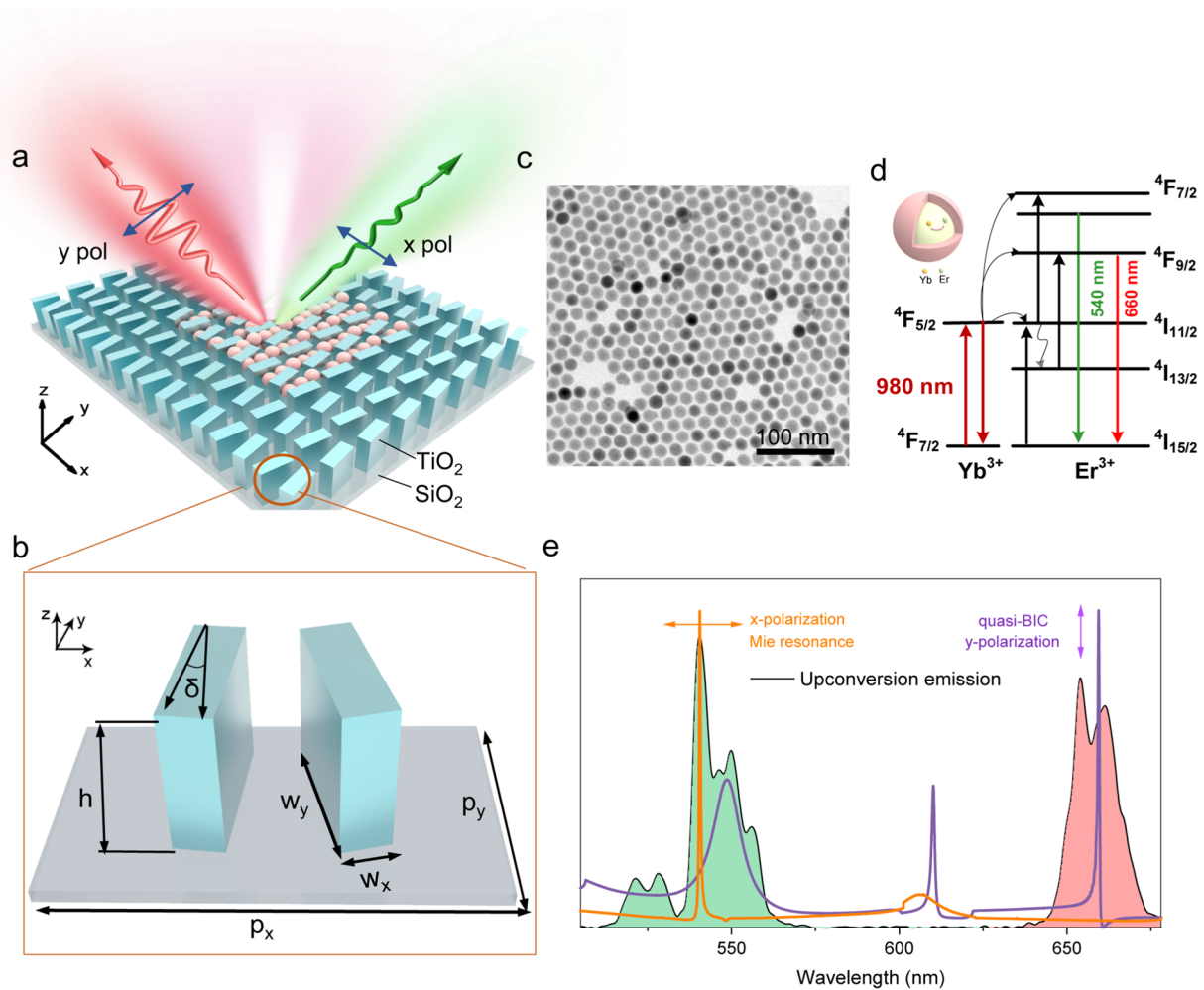


Fig. 1 Polarization-controlled upconversion emission enhancement. **a** Schematic presentation of a resonant metasurface with high-Q quasi-BIC and Mie resonant modes. The metasurface is composed of an array of TiO_2 nanobricks loaded with UCNPs. **b** Diagram of the designed unit cell depicting dual TiO_2 nanobricks with a tilt angle of $\delta = \pm 10^\circ$ relative to the y -axis, placed on a SiO_2 substrate. Geometrical parameters: $w_x = 100$ nm, $w_y = 240$ nm, $h = 450$ nm. The rectangular lattices periods are $p_x = 430$ nm and $p_y = 345$ nm. **c** TEM image of $\text{NaYF}_4:\text{Yb}/\text{Er}$ upconversion nanoparticles. **d** Energy level diagram illustrating the upconversion transition of $\text{Yb}^{3+}/\text{Er}^{3+}$. **e** x - and y -polarization controlled reflection spectra of the resonant metasurfaces overlapping with the emission spectra of the $\text{NaYF}_4:\text{Yb}/\text{Er}$ upconversion nanoparticles. Yellow curves denote Mie resonance under x -polarization and magenta curves denote quasi-BIC resonance under y -polarization incidence

red-shifts. A spectrally narrow resonance at ~ 660 nm can be observed for the case of $\delta = 10^\circ$, in which case the Q factor is calculated to be 1031.

For x -polarized normal incidence, multiple linewidth-vanishing BIC modes are identified in Fig. 2b, with different resonant wavelengths. Among them, a Mie resonance at 540 nm sustains as indicated by the green circle, regardless of variations in the asymmetry parameter δ . Moreover, the linewidth and resonance wavelength keep almost intact during the variation, as shown in Fig. 2b and Additional file 1: Fig. S3. We calculate the electromagnetic near field distributions and the multipole mode expansion spectra of the Mie resonance.

It reveals that the Mie resonance is dominated by the toroidal (TD) mode, with smaller contributions from other dipole modes, considering the lattice interaction and the influence of periodicity (Additional file 1: Fig. S4). Additional file 1: Fig. S5 illustrates that variations in other structural parameters (p_x , p_y , w_x , w_y , h and n) only affect the peak position of the Mie resonance. To match the emission wavelengths of the UCNPs, we judiciously adjust the asymmetric parameters to introduce high-Q resonances at 540 and 660 nm, respectively, responding to x - and y -polarizations. Along with resonance wavelength and polarization tunability, both the high-Q quasi-BIC and the Mie resonance mode strongly

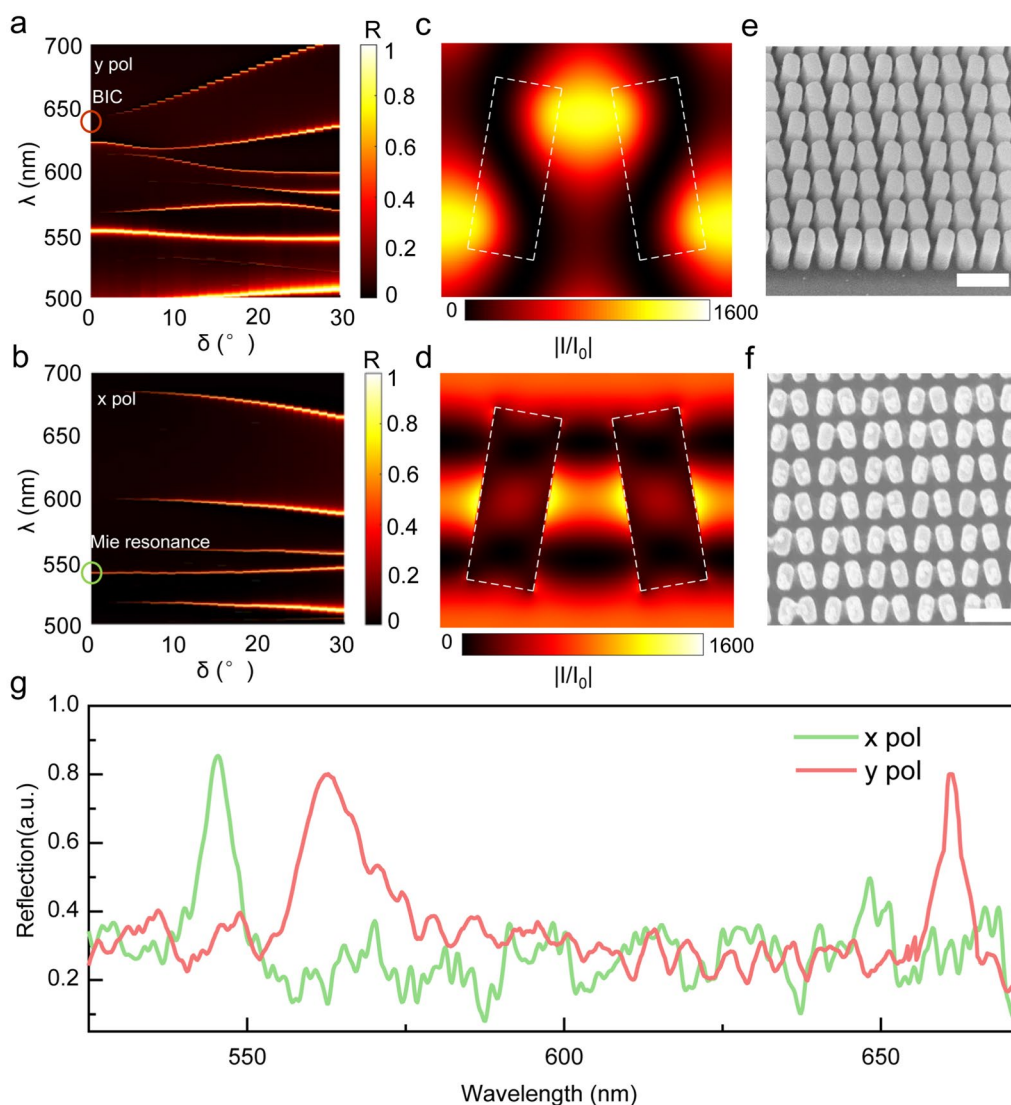


Fig. 2 **a–b** The evolution of reflection spectra by continuously varying the geometry asymmetry parameter δ under y-polarization **a** and x-polarization **b**. The vanishing point indicated by the red circle denotes the BIC mode. The green circle denotes the Mie resonance. **c–d** Electric field distributions at resonant wavelength 660 nm for y polarization, and 540 nm for x polarization. **e** Slant view SEM image of the resonant metasurface unloaded with UCNPs. **f** Top view SEM image of the resonant metasurface loaded with UCNPs. Scale bar: 500 nm. **g** The measured reflection spectra of the resonant metasurface under x- (green) and y- (red) polarizations, respectively

amplify the electric near fields around the resonators with intensity enhancement factors I/I_0 up to 1600 (Fig. 2c–d). This enables a strong confinement of the radiative emission field inside the metasurface, which exhibits a high field intensity for efficient upconversion luminescence enhancement.

The metasurface was fabricated using electron beam lithography (EBL) technology. Figure 2e shows slant-view scanning electron microscopy (SEM) images of the fabricated sample. $\text{NaYF}_4:\text{Yb/Er}$ (20/2 mol %) nanoparticles were uniformly spin-coated onto the metasurface, as shown in the top-view SEM image (Fig. 2f), and some of them were filled in TiO_2 nanobricks. The spectral measurement reveals that UCNPs/metasurface sample exhibit resonance peaks at ~ 540 and 660 nm under different polarizations, which perfectly overlap with the luminescence peaks of UCNPs (Fig. 2g). The experimentally achieved Q-factor of the Mie resonance mode at 540 nm is 151, and that of the quasi-BIC mode is around 268. The smaller values of

nanoparticles were uniformly spin-coated onto the metasurface, as shown in the top-view SEM image (Fig. 2f), and some of them were filled in TiO_2 nanobricks. The spectral measurement reveals that UCNPs/metasurface sample exhibit resonance peaks at ~ 540 and 660 nm under different polarizations, which perfectly overlap with the luminescence peaks of UCNPs (Fig. 2g). The experimentally achieved Q-factor of the Mie resonance mode at 540 nm is 151, and that of the quasi-BIC mode is around 268. The smaller values of

Q-factors compared with the theoretical ones are due to the finite array size and fabrication imperfections.

We further experimentally validated the feasibility of our design to achieve polarization-controlled upconversion emission enhancement. Figure 3a and b show the optical band structure of the resonant metasurface when the incident light is along the x - and y -direction, respectively. We note that x - and y -polarization incidences

show a clear response difference at the Γ point. The x -polarization incidences show strong reflection while y -polarization excitation shows nearly zero reflection at 540 nm, as indicated by the white circle. In contrast, the strong reflection in y -polarization excitation happens at 660 nm. The polarized upconversion luminescence from the UCNPs/metasurface sample was then collected by using home-made confocal system with discrimination

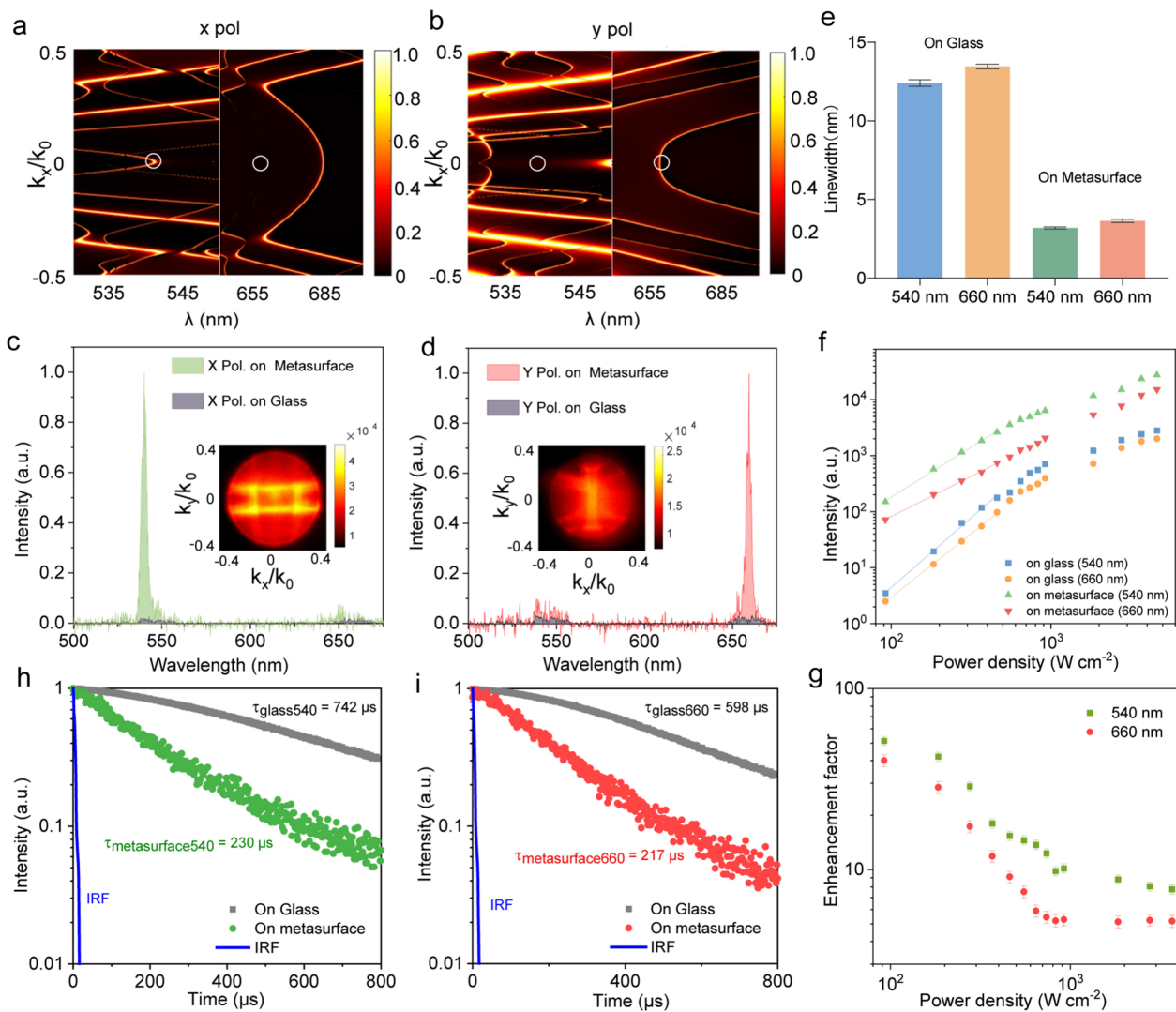


Fig. 3 **a–b** Simulated angle-resolved reflectance spectra under **a**) x -polarized beam and **b**) y -polarized beam for the wavelength range 530–700 nm. The ratio between the projected in-plane momentum k_x and free-space momentum k_0 indicates the reflection angle $\sin\theta = k_x/k_0$. **c–d** Upconversion luminescence spectra from UCNPs deposited on the metasurface and on glass substrate under x -polarization detection (c) and y -polarization detection (d). Inset: Fourier-plane upconversion photoluminescence images. **e**) The linewidth of luminescence spectra of UCNPs on the metasurface and glass substrate. **f**) The upconversion luminescence intensities from UCNPs deposited on glass and metasurface, as a function of the excitation power density for the green and red emissions, respectively. **g**) Luminescence enhancement factors at emission wavelengths of 540 nm (green) and 660 nm (red) as a function of the 980 nm incident excitation power. **h**) Emission lifetime measurements at 540 nm for UCNPs deposited on resonant metasurface supporting Mie resonant mode (green) and on a glass slide (black) under x -polarization detection. **i**) Time-resolved photoluminescence measurements of UCNPs deposited on a glass slide (black) and a metasurface supporting quasi-BIC mode (red) at an emission wavelength of 660 nm under y -polarization detection

capability (Additional file 1: Fig. S6). Under laser excitation power of 1 mW at wavelength 980 nm, the luminescence spectra of UCNPs on metasurface and glass are shown in Fig. 3c–d. Er^{3+} -activated UCNPs showed two characteristic bands centered around 540 and 660 nm. Compared to the luminescence intensity on the glass substrate, the UCNPs/metasurface sample exhibit sharp green emission in x -polarization detection. In contrast to glass, the luminescence intensity at 660 nm is significantly increased when detected in y -polarization. In the meantime, the Fourier-plane upconversion luminescence images at 540 and 660 nm were measured using a band-pass filter are shown in insets of Fig. 3c–d. The upconversion luminescence images display characteristic angle dispersion at dual bands, which implies that emissions of UCNPs are polarized and coupled to Mie resonance mode and the quasi-BIC mode of the resonant metasurface, respectively.

We found that the linewidth of fluorescence luminescence was significantly narrower compared to that on glass substrate. Figure 3e displays the statistical chart of the linewidths of the upconversion emission for UCNPs on the metasurface and on the glass substrate. The luminescence bandwidths at emission wavelengths 540 and 660 nm on the metasurface are 3.18 and 3.67 nm, respectively, which are close to the reflection spectrum bandwidth of the metasurface with UCNPs coating. In comparison to the upconversion fluorescence bandwidth on the glass substrate, the bandwidth on the metasurface is reduced by approximately four times. This finding offers new insights into narrowing linewidth of fluorescence emission for increasing fluorescence detection sensitivity and reducing background noise. Figure 3f illustrates the excitation power dependence of the UCNPs coupled metasurface and the reference samples. At low power excitation, both green and red emissions are present with slopes of 2.2 and 2.3, respectively, indicating that the upconversion emission is basically a two-photon process. It was observed that luminescence intensity increases linearly with incident power under strong excitation. However, the UCNPs coupled with the resonant metasurface exhibit a smaller slope and significant fluorescence enhancement due to the local field enhancement of the quasi-BIC mode and the Mie resonant mode. The upconversion emission rapidly reaches a saturation state, resulting in a reduced slope. Moreover, we quantified the enhancement factor for the upconversion luminescence intensity of each emission band under different excitation intensities (Fig. 3g). In high-power excitation, the enhancement factor is 7-fold for 540 nm and 5-fold for 660 nm due to the saturation, while it increases to 51-fold and 43-fold as the incident power is reduced to 92 Wcm^{-2} . The

enhancement factor is lower than that predicted mainly because of fabrication imperfections and uneven distribution of the nanoparticles.

The upconversion luminescence enhancements are typically attributed to a combination of multiple factors, namely the increased excitation rate result from both the absorption of the pump laser, and the radiative emission rate, which is enhanced by the Purcell effect at the emission wavelength. The physical mechanism behind the enhancement of upconversion fluorescence stems from the near-field enhancement induced by the quasi-BIC and Mie-resonant modes. The alterations in the electromagnetic field near the UCNPs may result in an excited flux, while the increased local density of optical states (LDOS) offers additional decay channels for the UCNPs to radiate via the quasi-BIC and Mie resonant modes into the far-field. To characterize the enhanced spontaneous-emission processes, we measured the radiative lifetime for the UCNPs-BIC sample and UCNPs on the reference glass (Fig. 3h–i). UCNPs on the resonant metasurface exhibit a decay rate enhancement of 3.2 at 540 nm. Simultaneously, the enhancement of the decay rate is 2.7 times greater than the glass sample at 660 nm.

The enhancement of the radiative decay rate of the resonant metasurface can also be explained through Purcell factor analysis, which was investigated by simulating a finite resonant metasurface with 30×30 unit-cells, consistent with the illumination spot diameter of $\sim 12 \mu\text{m}$ in the experiment. The corresponding Purcell factor of at 540 nm in x -polarized dipole orientation and 660 nm in y -polarized dipole orientation revealed the decay rate enhancement for green and red emissions, respectively (Additional file 1: Fig.S7). Only dipoles with a specific orientation will experience the Purcell effect, which is consistent with the polarization response of reflectance spectrum. It can be observed that the Purcell factor is very close to the changes in the emission decay rate. Furthermore, the Purcell factors at the electric field maxima at different positions are similar, suggesting that the quasi-BIC and Mie resonance with a large LDOS provide additional decay channels to enhance the decay rate and improve upconversion emission.

In addition to the radiative emission rate, we calculated the spectra for both x and y polarizations and the field enhancements in the wavelength range around 980 nm (Additional file 1: Fig. S8). It can be seen that no resonance peak appears around the 980 nm for both x and y polarization excitations. Most importantly, at excitation polarization angles varying from 0° to 90° , upconversion luminescence spectra of UCNPs coupled to the resonant metasurface as shown in Fig. Additional file 1: Fig. S8e–f. The fluorescence intensity does not change with the polarization of the 980 nm pumping light, suggesting

that the quasi-BIC mode and Mie resonance dominate the luminescence enhancement.

The inherent polarization-controlled high Q resonant modes in such resonant metasurface enables the selective manipulation of the dual-band emission polarizations. Figure 4a shows the polarized upconversion emission spectra of UCNPs on the metasurface, recorded by rotating an analyzer before the spectrometer. As the analyzer varies from 0° to 180°, the upconversion luminescence intensity of 540 and 660 nm on metasurface cross-change sinusoidally. The polar plot of the up-conversion luminescence intensity as a function of the polarization angle shows evident “8”-shaped convergence (Fig. 4c). The luminescence intensity at 540 nm shows a distinct *x*-polarized emission with the weakest and strongest emission at 0 and 90°, respectively. Conversely, the red emission at 660 nm shows the opposite case, indicating their countercyclical polarization anisotropy. On the glass substrate, the intensity of upconversion luminescence remains almost unchanged, and an approximate circle is drawn in polar plates, indicating no polarization response. The degree of polarization (DoP) of the upconversion luminescence can be evaluated as $\text{DoP} = (I_{\max} - I_{\min}) / (I_{\max} + I_{\min})$, where I_{\max} and I_{\min} represent the maximum and minimum values of upconversion

luminescence intensity. The luminescence emission of UCNPs on the reference glass shows no polarization sensitivity at all. In stark contrast, the luminescence emission DoP of UCNPs coupled with the resonant metasurface achieves ~0.86 and ~0.91 for emissions at 540 and 660 nm, respectively. The luminescence intensities of *x*- and *y*-components for green and red colors are selectively enhanced for UCNPs on the metasurface, respectively, providing a unique approach to achieve luminescence polarization control in nanophotonic devices.

In summary, we have demonstrated dual-band upconversion luminescence with simultaneously substantial augmentation and high degree of polarization from upconversion nanoparticles coupled to all-dielectric resonant metasurfaces. Supporting polarization-controlled quasi-BIC and Mie modes with ultra-high Q factors at dual upconversion bands, such resonant metasurfaces provides an enabling platform for significantly amplified upconversion emissions, achieving 51- and 43-fold enhancements, as well as simultaneous cross-polarized luminescence with DoP reaching 0.86 and 0.91, for green and red emissions, respectively. We notice that such NaYF₄:Yb/Er are not restricted to a special type of UCNPs, but they can be generalized to other types of UCNPs such as NaYF₄:Yb/Tm, as long as the resonance

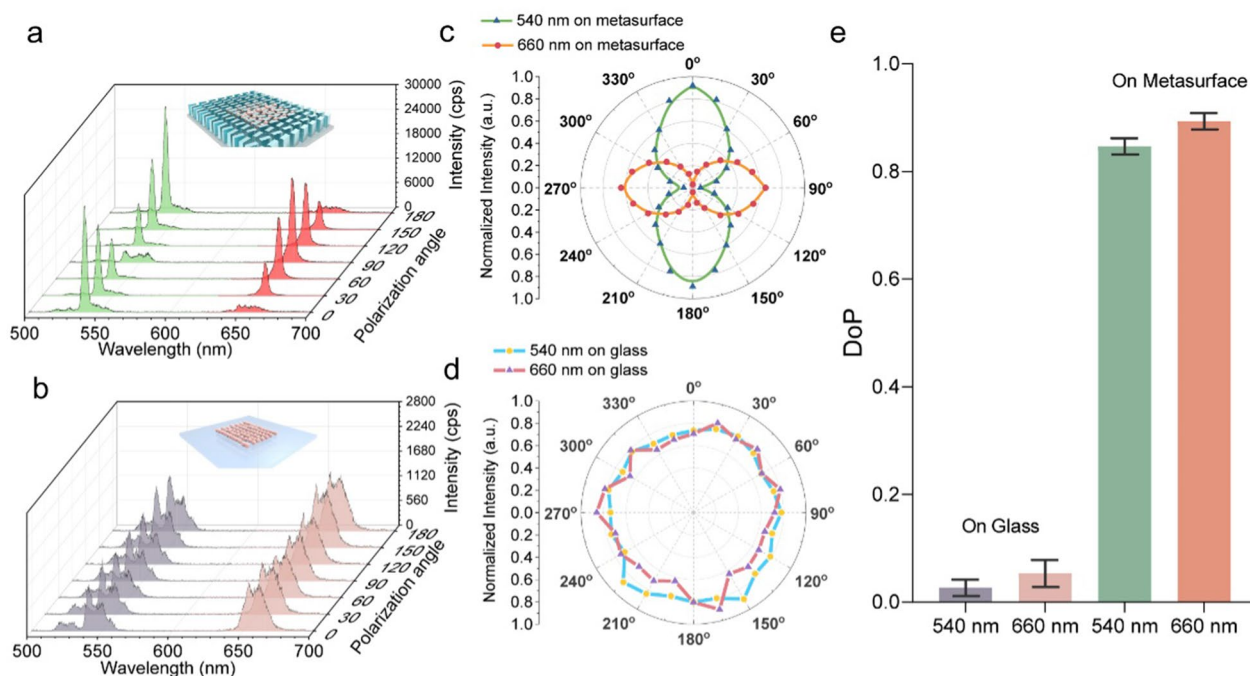


Fig. 4 **a** Upconversion luminescence spectra of UCNPs coupled to the resonant metasurface, recorded with a rotating analyzer at various angles from 0 to 180° in front of the spectrometer. **b** Upconversion emission spectra from UCNPs on a glass substrate, recorded at different detection polarization angles ranging from 0 to 180°. **c–d** Polar plots illustrating the luminescence intensity of UCNPs coupled to the metasurface **c** and UCNPs on a glass substrate **d** as functions of the emission polarization angle. **e** Degree of polarization (DoP) for upconversion luminescence of UCNPs on both metasurface and glass substrate

wavelengths of the metasurface are tailored to match the emission spectra of the chosen UCNP. High-doped UCNP (such as Tm^{3+}) have multiple energy levels, which is conducive to population establishment and cross-relaxation effect, and easier to realize population inversion. Coupling with polarization selective resonant metasurface is promising for efficient upconversion lasing with polarization controllability. We believe our results provide an excellent platform for ultrabright and polarized nanoscale emission sources holding great potential for the further advances in upconversion polarization lasing, biosensing, and fluorescence imaging.

3 Methods

3.1 Fabrication of samples

The metasurfaces were fabricated on a fused quartz substrate using a combination of processes, including electron beam lithography (EBL), atomic layer deposition (ALD), patterning, lift-off, and etching. First, the polymethyl methacrylate (PMMA) resist 950-A7 was spun on fused quartz substrate and baked at 180 °C for 2 min. The designed structures were patterned by using electron beam lithography system (6300FS, JEOL) and then developed in a mixture of MIBK and IPA with a ratio of 1:3. Then the TiO_2 film was deposited by the atomic layer deposition method. The ALD system is under continuous 20 sccm flow of N_2 carrier gas and maintained at 105 °C throughout the process. Finally, a dry etching process was performed in the ICP-RIE system (Plasmalab System 100 ICP180, Oxford) with a mixed reactive gas of BCl_3 and Cl_2 to remove the TiO_2 film on the top of the resist. And dry etching process with Oxygen also was used to remove the residual resist.

3.2 Characterization of metasurfaces

The broadband source (Fianium-WL-SC480) through a polarizer and half-wave plate generates different linear polarizations. The excitation beam is transmitted by beam splitters, then focused on the samples through an objective lens ($\text{NA}=0.4$). The reflection spectra of the resonant metasurface were measured using an Ocean spectrometer (USB4000).

3.3 Characterization of luminescence spectra and lifetime

Luminescence spectra were measured using a CW fiber-coupled laser diode ($\lambda_{ex}=980$ nm) as the excitation source. The objective lens with a numerical aperture (NA) of 0.4 was used for both excitation and emission collection. Then, the incident light was focused on the sample and the emission through polarizer and filter was captured by a spectrometer (Shamrock 303i, Andor) equipped with an

electron-multiplying charge-coupled device camera (EMCCD, Newtown, Andor). And time-resolved photoluminescence measurements of UCNP were performed by modulating the 980 nm laser with a signal generator. The luminescence is collected by a single-photon avalanche diode (SPAD; SPCM-AQRH-14-FC) and synchronized with a modulated excitation signal by a data acquisition (DAQ).

Supplementary Information

The online version contains supplementary material available at <https://doi.org/10.1186/s43593-023-00054-2>.

Additional file 1: Figure S1. Experimentally measured refractive index and light extinction ratio of the TiO_2 film. **Figure S2.** TEM image and corresponding size histogram of $\beta\text{-NaYF}_4\text{:Yb/Er}$ upconversion nanoparticles. **Figure S3.** Dependences of the Q-factor and resonant wavelength of the quasi-BIC mode **a** and another high-Q Mie-resonant mode **b** on the geometry asymmetry parameter δ . **Figure S4.** Multipole decomposition and nearfield electromagnetic patterns of the resonant metasurface. **a–b** Multipolar decomposition of the resonant metasurface at the quasi-BIC mode **a** and the Mie resonant mode **b**. **c–d** Near-field patterns of the quasi-BIC and Mie-resonant modes. **Figure S5.** Reflection spectra with the variation of other structural parameters for x-polarized normal incidences. **a–e** The reflection spectra with respect to the w_x , w_y , p_x , p_y and h for the resonance metasurface, respectively. **f** The reflection spectra with respect to the background refractive index. **Figure S6.** Optical setup for the characterization of upconversion emission. *SMF* single-mode fiber, *L1*, *L2* collimation lens, *BPF* bandpass filter. The linewidths of the 540 nm BPFs is 50 nm; The linewidths of the 655 nm BPFs is 60 nm; *M* mirrors, *FM* flexible mirror, *HWP* half-wave plate, *DM* dichroic mirror, *OL* objective lens, *SPAD* single-photon avalanche diode, *P* polarizer. **Figure S7. a–b** The relationship between the Purcell factor and the wavelength of UCNP deposited on the metasurface under x-polarized dipole orientation and y-polarized dipole orientation excitation. **c–d** Simulated Purcell factors for UCNP with different spatial locations on the metasurface at wavelengths 540 nm (**c**) and 660 nm (**d**), respectively. **Figure S8. a–b** Electric field distributions at resonant wavelength 980 nm for x polarization and y polarization. **c–d** Simulated reflection spectra of the resonant metasurface under x- and y-polarizations for 980 nm, respectively. **e** Upconversion luminescence spectra of UCNP coupled to the resonant metasurface, at excitation polarization angles varying from 0° to 90°, and x polarizer placed in the detection part. **f** Upconversion luminescence spectra of UCNP coupled to the resonant metasurface, at excitation polarization angles varying from 0° to 90°, and y polarizer placed in the detection part.

Acknowledgements

This work was supported by national Key R&D Program of China (2021YFB2802003, 2022YFB3607300), the China Postdoctoral Science Foundation funded project (No.2022M711241), National Natural Science Foundation of China (NSFC) (62075084), and the Guangdong Basic and Applied Basic Research Foundation (2022B151020004).

Author contributions

ZF and TS conceived the idea. ZF, TS, ZLD and XL designed the experiments. TS, and ZF carried out the design and simulation of the metasurfaces. ZF, TS, ZL, DYK and XL conducted the theoretical analysis of the results. GG and JL fabricated the samples. ZF and TS performed the measurements. ZLD, YK, and XL supervised the project. ZF, TS, ZLD and XL analyzed the data and wrote the paper. All authors participated in the discussion and analysis of the manuscript.

Availability of data and materials

All data needed to evaluate the conclusions in the paper are present in the paper and supporting information. Additional data related to this paper may be requested from the authors.

Declarations

Competing interests

Yuri Kivshar serves as an Editor for the Journal, no other author has reported any competing interests.

Received: 15 May 2023 Revised: 3 July 2023 Accepted: 13 July 2023

Published online: 18 September 2023

References

1. Y. Liu et al., Amplified stimulated emission in upconversion nanoparticles for super-resolution nanoscopy. *Nature*. **543**, 229–233 (2017)
2. Q. Zhan et al., Achieving high-efficiency emission depletion nanoscopy by employing cross relaxation in upconversion nanoparticles. *Nat. Commun.* **8**, 1058 (2017)
3. L. Liang et al., Continuous-wave near-infrared stimulated-emission depletion microscopy using downshifting lanthanide nanoparticles. *Nat. Nanotechnol.* **16**, 975–980 (2021)
4. Y. Liang et al., Migrating photon avalanche in different emitters at the nanoscale enables 46th-order optical nonlinearity. *Nat. Nanotechnol.* **17**, 524–530 (2022)
5. R. Pu et al., Super-resolution microscopy enabled by high-efficiency surface-migration emission depletion. *Nat. Commun.* **13**, 6636 (2022)
6. Y. Lu et al., Tunable lifetime multiplexing using luminescent nanocrystals. *Nat. Photonics*. **8**, 32–36 (2013)
7. Z. Feng et al., Laser-splashed plasmonic nanocrater for ratiometric upconversion regulation and encryption. *Adv. Opt. Mater.* **7**, 1900610 (2019)
8. R. Deng, F. Qin, R. Chen, W. Huang, M. Hong, X. Liu, Temporal full-colour tuning through non-steady-state upconversion. *Nat. Nanotechnol.* **10**, 237–242 (2015)
9. A. Fernandez-Bravo et al., Ultralow-threshold, continuous-wave upconverting lasing from subwavelength plasmons. *Nat. Mater.* **18**, 1172–1176 (2019)
10. B.-S. Moon, T.K. Lee, W.C. Jeon, S.K. Kwak, Y.-J. Kim, D.-H. Kim, Continuous-wave upconversion lasing with a sub-10 W cm⁻² threshold enabled by atomic disorder in the host matrix. *Nat. Commun.* **12**, 4437 (2021)
11. S. Brasselet, Fluorescence polarization modulation super-resolution imaging provides refined dynamics orientation processes in biological samples. *Light: Sci. Appl.* **11**, 322 (2022)
12. D.M. Jameson, J.A. Ross, Fluorescence polarization/anisotropy in diagnostics and imaging. *Chem. Rev.* **110**, 2685–2708 (2010)
13. X. Qin, A.N. Carneiro Neto, R.L. Longo, Y. Wu, O.L. Malta, X. Liu, Surface plasmon-photon coupling in lanthanide-doped nanoparticles. *J. Phys. Chem. Lett.* **12**, 1520–1541 (2021)
14. Y. Wu et al., Upconversion superburst with sub-2 μs lifetime. *Nat. Nanotechnol.* **14**, 1110–1115 (2019)
15. J. Xu et al., Multiphoton upconversion enhanced by deep subwavelength near-field confinement. *Nano Lett.* **21**, 3044–3051 (2021)
16. D. Bang et al., Asymmetric nanocrescent antenna on upconversion nanocrystal. *Nano Lett.* **17**, 6583–6590 (2017)
17. H. Chen et al., Sub-50-ns ultrafast upconversion luminescence of a rare-earth-doped nanoparticle. *Nat. Photonics*. **16**, 651–657 (2022)
18. H. He et al., Plasmonic chiral metasurface-induced upconverted circularly polarized luminescence from achiral upconversion nanoparticles. *ACS Appl. Mater. Interfaces*. **14**, 53981–53989 (2022)
19. Y. Meng et al., Bright single-nanocrystal upconversion at sub 0.5 W cm⁻² irradiance via coupling to single nanocavity mode. *Nat. Photonics*. **17**, 73–81 (2023)
20. W. Zhang, F. Ding, S.Y. Chou, Large enhancement of upconversion luminescence of NaYF₄:Yb³⁺/Er³⁺ nanocrystal by 3D plasmonic nano-antennas. *Adv. Mater.* **24**, OP236–OP241 (2012)
21. W. Park, D. Lu, S. Ahn, Plasmon enhancement of luminescence upconversion. *Chem. Soc. Rev.* **44**, 2940–2962 (2015)
22. A. Das, C. Mao, S. Cho, K. Kim, W. Park, Over 1000-fold enhancement of upconversion luminescence using water-dispersible metal-insulator-metal nanostructures. *Nat. Commun.* **9**, 4828 (2018)
23. Ā. Barreda, F. Vitale, A.E. Minovich, C. Ronning, I. Staude, Applications of hybrid metal-dielectric nanostructures: state of the art. *Adv. Photonics Res* **3**, 2100286 (2022)
24. J. He et al., Plasmonic enhancement and polarization dependence of nonlinear upconversion emissions from single gold nanorod@SiO₂@CaF₂:Yb³⁺,Er³⁺ hybrid core-shell-satellite nanostructures. *Light: Sci. Appl.* **6**, e16217 (2017)
25. S. Jahani, Z. Jacob, All-dielectric metamaterials. *Nat. Nanotechnol.* **11**, 23–36 (2016)
26. A.I. Kuznetsov, A.E. Miroshnichenko, M.L. Brongersma, Y.S. Kivshar, Luk'yanchuk B. Optically resonant dielectric nanostructures. *Science*. **354**, aag2472 (2016)
27. A.B. Evlyukhin et al., Demonstration of magnetic dipole resonances of dielectric nanospheres in the visible region. *Nano Lett.* **12**, 3749–3755 (2012)
28. G. Geng, W. Zhu, R. Pan, Z. Zhang, C. Gu, J. Li, Precise tailoring of multiple nanostructures based on atomic layer assembly via versatile soft-templates. *Nano Today*. **38**, 101145 (2021)
29. A. Tripathi et al., Metasurface-controlled photonic Rashba effect for upconversion photoluminescence. *Nano Lett.* **23**, 2228–2232 (2023)
30. F. Ding, S. Tang, S.I. Bozhevolnyi, Recent advances in polarization-encoded optical metasurfaces. *Adv. Photonics Res* **2**, 2000173 (2021)
31. C. Wu et al., Spectrally selective chiral silicon metasurfaces based on infrared fano resonances. *Nat. Commun.* **5**, 3892 (2014)
32. Y. Yang, I.I. Kravchenko, D.P. Briggs, J. Valentine, All-dielectric metasurface analogue of electromagnetically induced transparency. *Nat. Commun.* **5**, 5753 (2014)
33. A. Kodigala, T. Lepetit, Q. Gu, B. Bahari, Y. Fainman, B. Kanté, Lasing action from photonic bound states in continuum. *Nature*. **541**, 196–199 (2017)
34. A. Tripathi et al., Topological nanophotonics for photoluminescence control. *Nanophotonics*. **10**, 435–441 (2020)
35. C.W. Hsu et al., Observation of trapped light within the radiation continuum. *Nature*. **499**, 188–191 (2013)
36. K. Koshelev, S. Lepeshov, M. Liu, A. Bogdanov, Y. Kivshar, Asymmetric metasurfaces with high-Q resonances governed by bound states in the continuum. *Phys. Rev. Lett.* **121**, 193903 (2018)
37. Z. Liu et al., High-Q quasibound states in the continuum for nonlinear metasurfaces. *Phys. Rev. Lett.* **123**, 253901 (2019)
38. F. Yesilkoy et al., Ultrasensitive hyperspectral imaging and biodetection enabled by dielectric metasurfaces. *Nat. Photonics*. **13**, 390–396 (2019)
39. T. Shi et al., Planar chiral metasurfaces with maximal and tunable chiroptical response driven by bound states in the continuum. *Nat. Commun.* **13**, 4111 (2022)
40. S.I. Azzam et al., Single and multi-mode directional lasing from arrays of dielectric nanoresonators. *Laser Photonics Rev* **15**, 2000411 (2021)
41. M. Wu et al., Room-temperature lasing in colloidal nanoplatelets via Mie-resonant bound states in the continuum. *Nano Lett.* **20**, 6005–6011 (2020)
42. X. Zhang, Y. Liu, J. Han, Y. Kivshar, Q. Song, Chiral emission from resonant metasurfaces. *Science*. **377**, 1215–1218 (2022)